Observations of Gap Flow in the Wipp Valley on 20 October 1999: Evidence of Subsidence

TOMISLAV MARIĆ AND DALE R. DURRAN

Department of Atmospheric Sciences, University of Washington, Seattle, Washington

(Manuscript received 19 July 2007, in final form 2 October 2008)

ABSTRACT

Using extensive observations collected from various platforms around the Brenner Pass in the Austrian Alps during the Mesoscale Alpine Programme, a detailed description of the kinematic and thermodynamic structure of the shallow-foehn event that occurred on 20 October 1999 in the Wipp Valley is constructed. Downstream of the gap the flow develops a well-mixed surface layer capped by a relatively strong temperature inversion of 5–6 K. Such inversions are often assumed to be kinematically similar to the free surface at the top of a liquid; however, the data suggest the presence of strong subsidence through the mean position of the inversion layer capping the flow. Such subsidence is supported by in situ aircraft observations and Doppler lidar measurements but is not consistent with the observed turbulent heat fluxes, which are too small to account for the diabatic heating required by the isentrope-relative downward velocities. The 1-Hz time resolution of the P3 data may, however, be too coarse to correctly capture the full turbulent heat flux.

1. Introduction

Gap winds are jets of air that are channeled by topographic features such as mountain passes, river canyons, or gaps between mountainous islands. Relatively few measurements have been collected above the surface during gap wind events. In situ aircraft observations, for example, are difficult to obtain because the plane must sample a turbulent high-speed flow in close proximity to the terrain. Not surprisingly, those cases where aircraft observations have been collected involve relatively wide gaps such as the Shelikof Strait (Lackmann and Overland 1989) and the Strait of Juan de Fuca (Colle and Mass 2000). Detailed observations of the above-surface flow in a narrow gap were finally obtained in the Wipp valley (Wipptal), during the Mesoscale Alpine Programme (MAP), where observations were taken by aircraft, lidars, dropsondes, and a Doppler sodar (Mayr et al. 2004).

Several analyses of gap winds using the MAP data collected in the Wipptal have recently appeared. Gohm et al. (2004) used data from 24 and 25 October 1999 to perform a careful verification of high-resolution numerical simulations of that event. Weissmann et al. (2004) used Doppler lidar along with other data sources to document the temporal evolution and small-scale spatial structure of gap flow during shallow and deep foehn on 2 and 3 October 1999. Flamant et al. (2002) compared observations of the 30 October 1999 shallow foehn with very high-resolution numerical simulations to create a comprehensive picture of the flow. They also diagnosed parameters relevant to the reduced-gravity shallow-water (RGSW) model from the numerical simulations and found that the observed and simulated hydraulic jumps within the valley did appear to correspond to transitions from sub- to supercritical regimes in the RGSW sense.

The RGSW model assumes that the gap-wind layer is well mixed and topped by a sharp jump in density that is dynamically equivalent to the free surface at the upper boundary of a liquid subject to the reduced gravitational restoring force $g' = g\Delta\theta/\bar{\theta}$, where $\Delta\theta$ is the jump in potential temperature at the top of the mixed layer and $\bar{\theta}$ is a potential temperature representative of the gap flow itself. The RGSW framework is attractive because it accounts for nonlinear processes in a relatively simple manner. The predictions from RGSW theory were compared to surface and radiosonde observations in several studies prior to MAP (Arakawa 1968; Pettre 1982; Jackson and Steyn 1994; Dorman et al. 1995).

Corresponding author address: Dale R. Durran, Dept. of Atmospheric Sciences, University of Washington, Box 351640, Seattle, WA 98195–1640.
E-mail: durrand@atmos.washington.edu

DOI: 10.1175/2008JAS2568.1

© 2009 American Meteorological Society

Gohm and Mayr (2004) simulated the flow in the Wipptal using a time-dependent nonlinear shallow-water model and found that the simulated winds and the positions of the hydraulic jumps were generally in good agreement with observations, including as a specific example the 20 October 1999 case considered in this paper. However, they report that in some cases the governing parameters for the model (e.g., reduced gravity) could not be determined unambiguously from the observations because the increase in density above the gap flow was not concentrated in a sharp elevated inversion that was well defined and uniform over the domain. Recently, Armi and Mayr (2007) found that RGSW theory provided a good model for the foehn flow on 2 October 1999 and also well downstream of the Brenner Pass on 20 October 1999, but in the vicinity of the pass the flow in the latter case was better described by a continuously stratified hydraulic model.

In this study we present a detailed analysis of the gap flow on 20 October 1999 using data from an extensive set of remote and in situ sensors deployed in and above the Wipptal during the MAP experiment. The availability of data from such a wide variety of different observational platforms allows us to extend the previous analyses of this event (Gohm and Mayr 2004; Armi and Mayr 2007) by comparing observations taken by the National Atmospheric and Oceanic Administration's (NOAA's) P3 aircraft over a 2-h period with data collected almost instantaneously by lidars and dropsondes to verify that the flow sampled by the P3 was almost steady. Interpreting the P3 data as an approximately instantaneous snapshot of the flow in a vertical plane above the axis of the Wipptal, further analysis of the P3 observations of velocity and potential temperature reveals evidence of significant subsidence at the level of the inversion capping the high-speed flow.

2. The data sources

Extensive meteorological measurements from a dense network of different platforms were obtained in the Wipptal during the MAP special observing period (SOP; Bougeault et al. 2001). An overview of gap-flow measurements in the Wipptal is given by Mayr et al. (2004). During MAP, 35 automatic weather stations taking hourly measurements of temperature, wind, pressure, and humidity were located in the Brenner Pass target area. In addition to routine soundings from Innsbruck, radiosondes were launched on days with strong foehn from Sterzing and Gedeir (see Fig. 1a).

The Austrian Zentralanstalt für Meteorologie und Geodynamik (ZAMG) installed a "Phased Array 2" (PA2) Doppler sodar at Brennerbad, about 4 km south of the Brenner Pass (see Fig. 1a). During MAP the PA2 was measuring winds in vertical gates with 25-m steps, averaged over 30-min time intervals. Because of reflections from the nearby valley sidewalls and strong background noise produced by the traffic over the Brenner Pass, the maximum vertical range of the sodar was limited to about 500 m above ground.

The NOAA WP-3D (P3) flew within the gap-wind layer, along flight tracks parallel to the Wipptal axis, between approximately 1030 and 1330 UTC 20 October 1999. The complete description of the P3 measurements and technical characteristics of its instruments can be found at the NOAA Aircraft Operations Center web page (http://www.aoc.noaa.gov). During MAP, a scanning aerosol backscatter lidar (SABL), developed by the Atmospheric Technology Division (ATD) of the National Center for Atmospheric Research (NCAR), was operated on board the Electra aircraft in nadir-pointing mode. In this study we used 1-Hz SABL data from the green channel (532 nm), which had vertical resolution of 7.5 m and average horizontal resolution of 120 m, to determine the location of the top of the atmospheric boundary layer (ABL). In addition to the SABL observations, the Electra released a few dropsondes, one of which landed in a favorable location in the southern part of the Wipptal, halfway between the Brenner Pass and Gedeir (see Fig. 1a).

NOAA's Environmental Technology Laboratory operated a scanning Doppler lidar, TEACO2, near Gedeir (see Fig. 1a). Because the airflow tends to be channeled by the Wipptal to follow roughly the north–south valley axis through the lidar site, the radial wind velocities retrieved by the TEACO2 roughly approximate the actual winds in the valley during shallow foehn events. For this study we used sets of consecutive scans to produce three-dimensional (3D) volume data pointing either upstream toward the Brenner Pass (at average 178° azimuth) or downstream toward Innsbruck (at average 320° azimuth). It takes approximately 6 min to complete an individual volume scan. The advantage of using 3D lidar data is that arbitrary cross sections through the volume can be examined. A detailed comparison between wind speeds measured in situ by the P3 in the Wipptal and those obtained from the TEACO2 lidar was performed by Durran et al. (2003). They found a bias in which the P3 wind speeds exceeded those from the TEACO2 lidar by 2.4 m s^{-1} when the lidar was scanning up valley and by 0.4 m s^{-1} when the lidar was scanning down valley. For the analyses in this paper, the TEACO2 data were adjusted to facilitate comparison with the P3 observations by removing these biases. The lidar data were also quality controlled by removing all returns with backscatter values less than 28 dB.

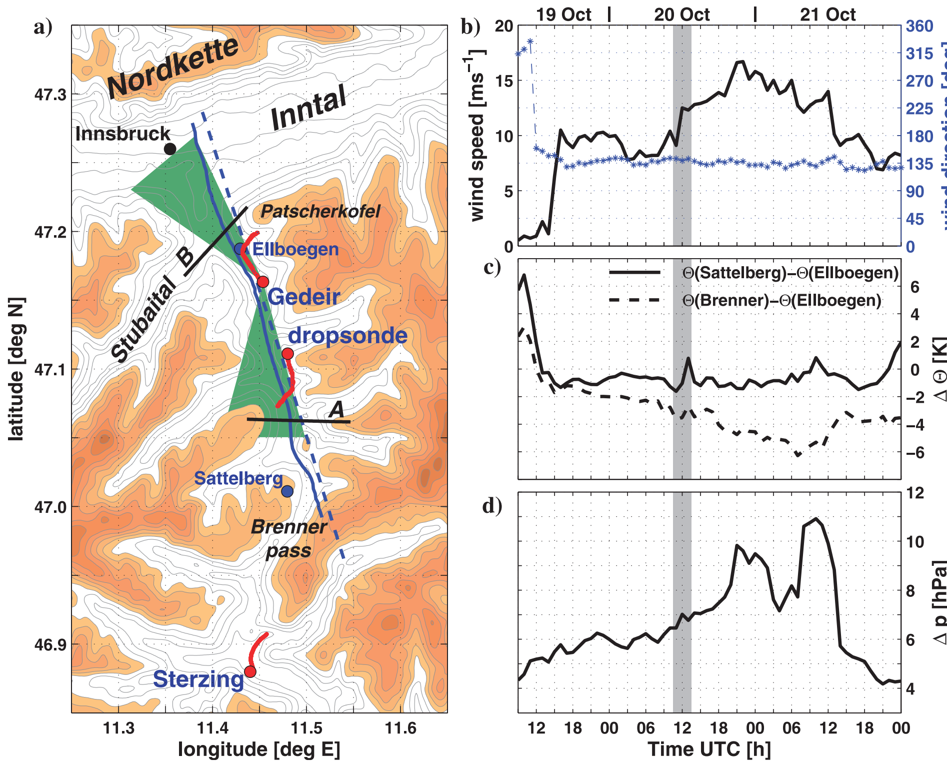

FIG. 1. (a) Map of the Wipptal. Terrain contours are every 200 m with elevations greater than 1800 m filled. Green-shaded triangles indicate the footprint of the TEACO2 Doppler lidar scans. Heavy solid blue line shows the projection onto the surface of the average P3 flight track on 20 Oct 1999. (Northernmost and southernmost 3 km of this track are averages for just the upper-level legs.) Dashed blue line indicates the ground track of the NCAR Electra between 1215 and 1220 UTC. Solid black lines marked A and B show the portions of the Electra flight tracks crossing the Wipptal between 1334:15 and 1335:05 UTC (track B), and between 1321:29 and 1322:28 UTC (track A). Red lines indicate trajectories of the sounding balloons between the surface and 3500 m above the ground. (b)–(d) Foehn evolution between 0900 UTC 19 Oct and 0000 UTC 22 Oct 1999 as recorded at surface weather stations: (b) wind speed (solid black) and direction (dashed blue) in Ellboegen; (c) differences in potential temperature between Sattelberg and Ellboegen, and between Brenner and Ellboegen; (d) difference between the pressure in Sterzing and Ellboegen. The gray-shaded area in (b)–(d) indicates the time of the P3 observations.

3. Event overview

a. Synoptic scenario

The 20 October 1999 MAP IOP 8 case started as a shallow foehn with the approach of a pressure trough from the west. Surface winds in the Wipptal and surrounding peaks turned southerly around 1200 UTC 19 October. Maximum winds were observed from late in the afternoon on 20 October through early morning on 21 October as the axis of the upper-level trough approached the western flank of the Alps and a transition to deep foehn occurred. On the afternoon of 21 October 1999 the surface cyclone propagated to the north of the Alps, bringing relatively colder air to the region, reducing the north–south pressure gradient and the wind speed in the Wipptal, and marking the end of the event.

b. Topographic environment

The Brenner Pass (1373 m MSL) is one of the deepest incisions in the Alpine range and is situated in the Wipp Valley (Wipptal), which is shown in Fig. 1a. It stretches in a north–south direction from Sterzing/Vipiteno (950 m MSL) in Italy to Innsbruck (600 m MSL) in Austria, with a total length of about 50 km. To the north, the Wipptal merges with the east–west-aligned Inn Valley (Inntal) and is bounded by the Nordkette mountain range (average elevation of 2400 m MSL). The Wipptal is also connected to several side valleys, the largest of which are Stubaital and Gschnitztal. The Brenner Pass has a double-gap structure; the base of the lower gap is at approximately 1400 m MSL and is 2 km wide. The upper gap's base is at 2100 m MSL and is 15 km wide, whereas the average elevation of the neighboring ridges is 3000 m MSL.

c. Surface wind and potential temperature

Figures 1b–d show the evolution of the 20 October 1999 foehn event based on the data from surface weather stations in Sterzing (944 m MSL), Brenner (1373 m MSL), Sattelberg (2108 m MSL), and Ellboegen (1080 m MSL). Ellboegen is situated in the lower end of the Wipptal, about 10 km south-southeast of Innsbruck (see Fig. 1a). It is representative of the foehn conditions in the exit region of the valley and is known for reporting relatively high wind speeds. Sattelberg is a mountain station located near Brenner at an elevation about halfway between the pass and the main Alpine crest and is representative of the airflow through the upper gap. Figure 1b shows wind speed (solid black line) and direction (dashed blue line) at Ellboegen. The wind direction changed from north to south-southeast and the wind speed increased significantly around 1200 UTC 19 October 1999, marking the onset of the shallow foehn. It remained relatively unchanged at about 10 m s^{-1} until 1200 UTC 20 October, when the flow accelerated up to 13 m s^{-1}. The speed then remained relatively steady throughout the afternoon until the transition to deep foehn occurred at approximately 1900 UTC 20 October. The wind speed peaked at 17 m s^{-1} early during the deep foehn phase and then gradually decreased throughout the rest of the period.

Simultaneous to the onset of southerly flow in the Wipptal, the potential temperature difference between Sattelberg and Ellboegen [θ(Sattelberg) $-$ θ(Ellboegen)], shown in Fig. 1c, dropped and remained around -1 K during the duration of the event. Although Sattelberg is 1028 m higher than Ellboegen, its potential temperature is lower, implying that if the airflow past Ellboegen were isentropic, the airstream must have subsided from a higher level than the elevation of Sattelberg. Previous analyses of the shallow foehn in the Wipptal on 2 October (Weissmann et al. 2004) and 30 October (Mayr et al. 2004) also show the potential temperature at Ellboegen exceeding that at Sattelberg during the foehn event. Additional evidence that the air passing though Ellboegen must have subsided from aloft and not simply traveled through the Brenner Pass is provided by the curve in Fig. 1c showing the potential temperature at the Brenner Pass minus that at Ellboegen, which is negative during the entire event and reaches an extreme value during the deep foehn phase of -6 K at about 0600 UTC 21 October 1999.

Figure 1d shows the pressure difference between Sterzing and Ellboegen: $\Delta p = p(\text{Sterzing}) - p(\text{Ellboegen})$. The surface pressure from the Ellboegen station was reduced to the Sterzing level (136 m vertical distance) using the temperature profile from the Innsbruck sounding. High winds at Ellboegen are positively correlated with a northward Sterzing-to-Ellboegen pressure gradient; the correlation coefficient for the period shown in Fig. 1d is 0.74. Comparable or slightly higher correlation coefficients were reported for other south foehn cases during MAP, such as on 24 October 1999 (Gohm et al. 2004).

In summary, the 20–22 Oct 1999 south foehn case produced the largest pressure differences between Sterzing and Ellboegen (11 hPa) recorded during the entire MAP SOP (7 September–16 November 1999). It also resulted in very strong warming between the upper pass and lower Wipptal, where the potential temperature at Ellboegen was almost 2 K higher than at Sattelberg. The maximum wind speeds observed at surface weather stations in the Wipptal peaked at about 17 m s^{-1} in Ellboegen and over 25 m s^{-1} on the surrounding crests.

d. Vertical and horizontal structure of the flow

Figure 2 shows the vertical profile of temperature, wind speed, and mixing ratio recorded at approximately 1200 UTC 20 October 1999 by soundings released from Sterzing and Gedeir, and from a dropsonde released from the Electra at 1323 UTC that reached the valley floor about halfway between the Brenner Pass and Gedeir (see Fig. 1a for locations). Both upstream and downstream of the Brenner Pass, the layer near the surface is very well mixed and between 1000 and 1250 m deep. The thickness of the well-mixed surface layer decreases as the air flows from Sterzing over the pass and down the valley. In the Wipptal, both the dropsonde and Gedeir soundings show a surface layer capped by a relatively strong elevated inversion with a temperature step of about $\Delta\theta = 5$ K over a 250-m layer (2250–2500 m MSL) in the dropsonde data and about $\Delta\theta = 6$ K over a 500-m layer (2150–2650 m MSL) at the Gedeir location. Instead of an elevated inversion above the surface layer, in the Sterzing profile there is a deep layer of enhanced stability between 2150 and 3250 m MSL. All three soundings show a second elevated temperature inversion at approximately 4000 m MSL and a layer with typical tropospheric stratification above.

The wind profiles show strong acceleration between Sterzing and the sites in the Wipptal throughout the layer between the surface and the inversion. Maximum wind speeds in the dropsonde and the Gedeir sounding are between 16 and 19 m s^{-1} and the direction is from the south or south-southeast, along the Wipptal channel. Above the inversion, the winds in the Wipptal soundings are significantly slower (6–10 m s^{-1}) and the direction is from the southwest and west. In contrast, the winds between the surface and 2100 m MSL at Sterzing do not exceed 4 m s^{-1} and are mostly from the west and

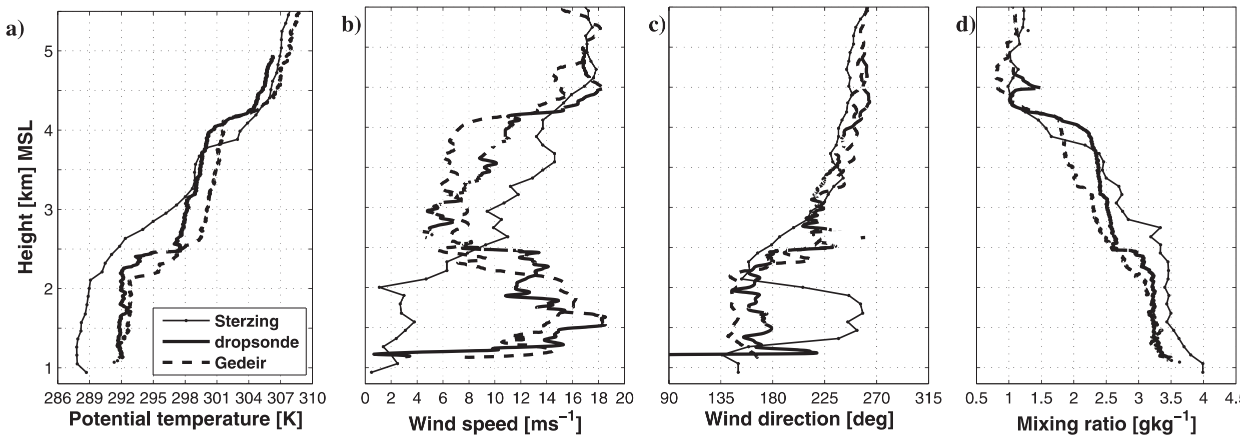

FIG. 2. Sterzing, dropsonde, and Gedeir soundings at approximately 1200 UTC 20 Oct 1999: (a) potential temperature, (b) wind speed, (c) wind direction, and (d) mixing ratio.

southwest. Further aloft the winds at Sterzing are in the same direction but are somewhat stronger than those in the Wipptal.

The weak winds at Sterzing suggest that the air upstream of the pass in the layer between 1250 and 2000 m MSL was partially blocked. Such blocking is consistent with the decrease in the low-level mixing ratios between the Sterzing sounding upstream and the dropsonde and Gedeir sounding downstream. In addition, partial blocking of the low-level flow is suggested by the relative weakness of the winds in the narrow region of the Brenner Pass. As shown by the Doppler sodar measurements in Fig. 3, around 1200 UTC 20 October 1999 the wind speeds above the pass were 8–10 m s^{-1}, which is about half the strength of the low-level winds measured by the dropsonde and the Gedeir sounding.[1] If the flow through the Brenner Pass supplied all the air in the high-speed current in the lower Wipptal, mass conservation would require the winds in the narrow pass to be much stronger than those where the valley widens downstream, which is certainly not the case.

The finding that the high-speed flow in the Wipptal descends from at least the level of the upper gap (about 700 m higher than the Brenner Pass itself) has been previously documented in several studies (Mayr et al. 2004; Flamant et al. 2002; Armi and Mayr 2007). On the other hand, previous authors do not appear to have discussed the possibility that even well downstream of the pass and the main Alpine crest, the gap flow continues to be fed by air subsiding from aloft; this will be investigated in section 5.

[1] The wind speed at the Brenner Pass did increase later in the day as the transition to deep foehn occurred. A maximum of about 15 m s^{-1} at 400 m AGL was recorded by the sodar around 0600 UTC 21 October 1999, at the peak of the deep foehn.

Figure 4 shows the TEACO2 lidar-retrieved radial wind interpolated to a horizontal plane at 1580 m MSL (about 500 m above the ground at Gedeir) from volume scans obtained approximately at (left) 1130 and (right) 1330 UTC 20 October 1999. At both 1130 and 1330 UTC a cross-valley asymmetry is present, with significantly stronger winds above the eastern side of the Wipptal. This asymmetry is evident throughout the valley but is especially pronounced downstream of Gedeir. The tendency for gap flows to be stronger on the eastern side of the Wipptal has been attributed to the presence of southwesterly flow aloft (Flamant et al. 2002) or the curvature of the valley axis (Gohm and Mayr 2004; Gohm et al. 2004). Between 1130 and 1330 UTC, the wind speeds in the lower part of the valley (downstream of the lidar) increased by approximately 15%–20%, whereas in the upper part of the valley the increase was much less pronounced, both at the surface stations and in the lidar scan. The maximum winds (exceeding 21 m s^{-1}) occurred near the exit of the Wipptal, about 500 m above ground, and were approximately 30% stronger than the winds on surrounding crests (shown by red arrows in Fig. 4).

4. Verification of the temporal stationarity of the P3 cross-sectional data

On 20 October 1999 the P3 aircraft was taking in situ measurements in the Wipptal between 1038 and 1322 UTC. Most of the P3 flight tracks were vertically stacked above the axis of the valley, almost directly above the average ground track shown in Fig. 1a. Provided the gap flow was sufficiently stationary, the data collected along these different flight tracks can be combined into a single 2D cross section to give a richly detailed description of the atmospheric structure within

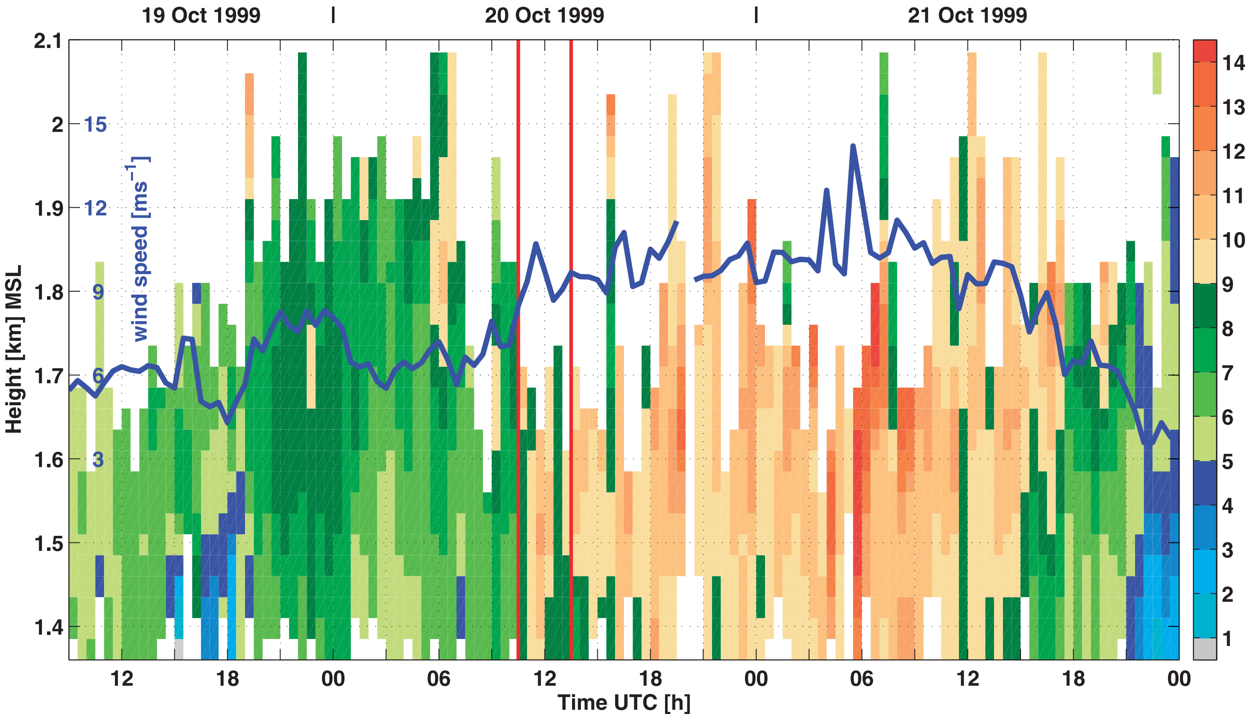

FIG. 3. Doppler sodar-retrieved winds (m s^{-1}) over the Brenner Pass between 0900 UTC 19 Oct and 0000 UTC 22 Oct 1999. Solid blue line and the corresponding scale show the wind speed averaged in the vertical between 1400 and 1600 m MSL. Vertical red lines mark the times when TEACO2 Doppler lidar and the P3 collected measurements.

the Wipptal. We have constructed vertical cross sections based primarily on nine flight tracks completed over the roughly 1.5-h interval between 1154 and 1322 UTC.[2] As discussed earlier, this was a period when the surface wind speeds in the Wipptal were relatively steady, just after the period of acceleration that ended about 1200 UTC 20 October 1999. We can further assess the stationarity of the flow sampled along these flight tracks by comparing subsets of the P3 observations with measurements collected much more rapidly by the TEACO2 scanning Doppler lidar, the SABL backscatter lidar on the Electra, the dropsonde, and the Gedeir radiosonde.

Figures 5a,b shows a comparison of the P3- and TEACO2-retrieved radial winds. The TEACO2 observations were collected as part of volume scans conducted between roughly 1320 and 1330 UTC. The P3 data were interpolated to create a vertical cross section as follows: The component of the P3-measured wind velocity in the direction of the lidar beam $\upsilon_r(x,z)$, was computed at each data point and then interpolated to a regular grid, with horizontal and vertical resolution $\Delta x = 250$ m and $\Delta z = 50$ m, using the algorithm proposed by Smith and Wessel (1990), which solves

$$(1-T)\nabla^2(\nabla^2\upsilon_r) + T\nabla^2\upsilon_r = \sum_i \upsilon_{r,i}\delta(x-x_i)\delta(z-z_i), \quad (1)$$

where $\upsilon_{r,i}$ is the observed radial wind at point (x_i,z_i) and $T = 0.25$ is a "tension factor" empirically determined to avoid spurious oscillations and false extrema inside the domain. The P3 observations $\upsilon_{r,i}$ are also plotted as colored dots along each flight leg in Fig. 5a using the same color scale as for the interpolated field; these dots are almost invisible, indicating that the interpolation procedure is faithfully preserving the actual data values along each flight leg.

As is apparent in Figs. 5a,b, the agreement between the P3 and TEACO2 lidar data is very good. In the lower part of the Wipptal (downstream of the lidar) both cross sections show a jet of fast flow near the surface with much weaker wind aloft. Above the jet, the P3 data show small regions of stagnant and even reversed flow, which is not as pronounced in the lidar-retrieved wind. The location (angle and elevation) of the shear layer capping the jet is almost identical in the both datasets. The maximum wind speed in both the P3 and TEACO2 cross sections is 21 m s^{-1} and occurs

[2] One additional track, flight track 2 from 1.5 h earlier in the event, was also used to fill a large void in the data between tracks 1 and 3 (see Fig. 5).

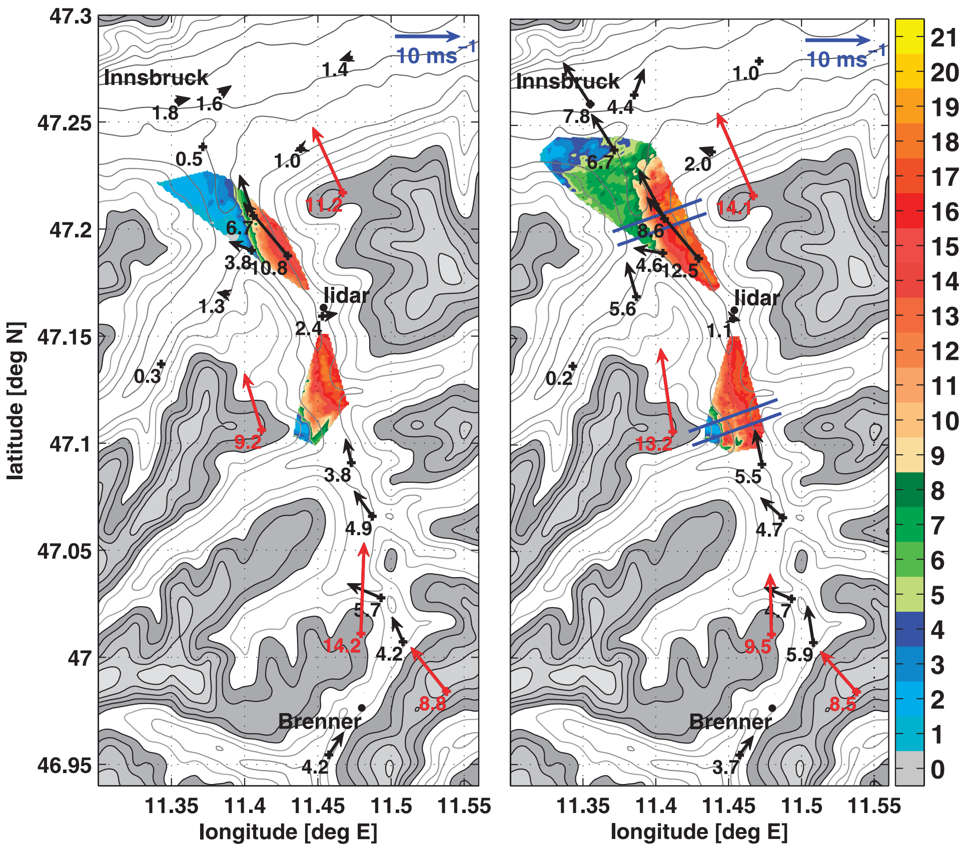

FIG. 4. Radial wind retrieved from TEACO2 Doppler lidar volume scans interpolated to horizontal plane at 1580 m MSL shown by color fill. Topographic contours are every 200 m, with gray shading at elevations above 1800 m. Radial wind from volume scans are shown at approximately (left) 1130 and (right) 1330 UTC 20 Oct 1999. Arrows and associated numbers indicate wind speed measured at surface stations. Red arrows are used for stations on surrounding peaks and valley walls. Parallel blue lines show the locations of the lidar cross sections in Fig. 11.

downstream of the lidar approximately 400 m above the ground. Upstream of the lidar the agreement is not as impressive and there is a lot of missing data in the lidar cross section. The maximum wind speed upstream of Gedeir in the P3 cross section is 19 m s^{-1}; the lidar measured a slightly weaker speed of 17 m s^{-1}. Nevertheless, the overall structure of the wind field in both datasets is the same. Both the lidar and P3 data show similar regions of fast flow between the ground and approximately 2 km MSL.

Isentropes constructed from the P3 observations are compared with SABL backscatter data in Fig. 5c. The potential temperatures were interpolated from the P3 data using the same method as for the lidar-radial winds. The SABL data were collected between 1215 and 1220 UTC as the Electra flew at an altitude of approximately 5 km MSL along a track almost coincident with the average ground track of the P3 (see Fig. 1a). Because the SABL backscatter measurements were rather noisy, the original data were filtered with a Butterworth low-pass filter designed to remove wavelengths shorter than 400 m in the vertical (approximately 1/4 of the average depth of the observed mixed aerosol layer) and wavelengths shorter than 900 m in the horizontal (approximately 1/4 of the wavelength of the undulations of the top of the aerosol layer). The filtered data were used to calculate the vertical gradients of the backscatter intensity and to estimate the elevation of the top of the aerosol mixed layer, which was taken as the point where the magnitude of the gradient in the backscatter intensity was a maximum. Because the aerosol mixed layer was not homogeneous but usually contained several individual layers, a secondary maximum was very occasionally interpreted as the top of the main aerosol layer to better maintain continuity with adjacent regions. Also note that the SABL beam was blocked by shallow clouds at about 3.7 km MSL, 5–10 km upstream of Gedeir.

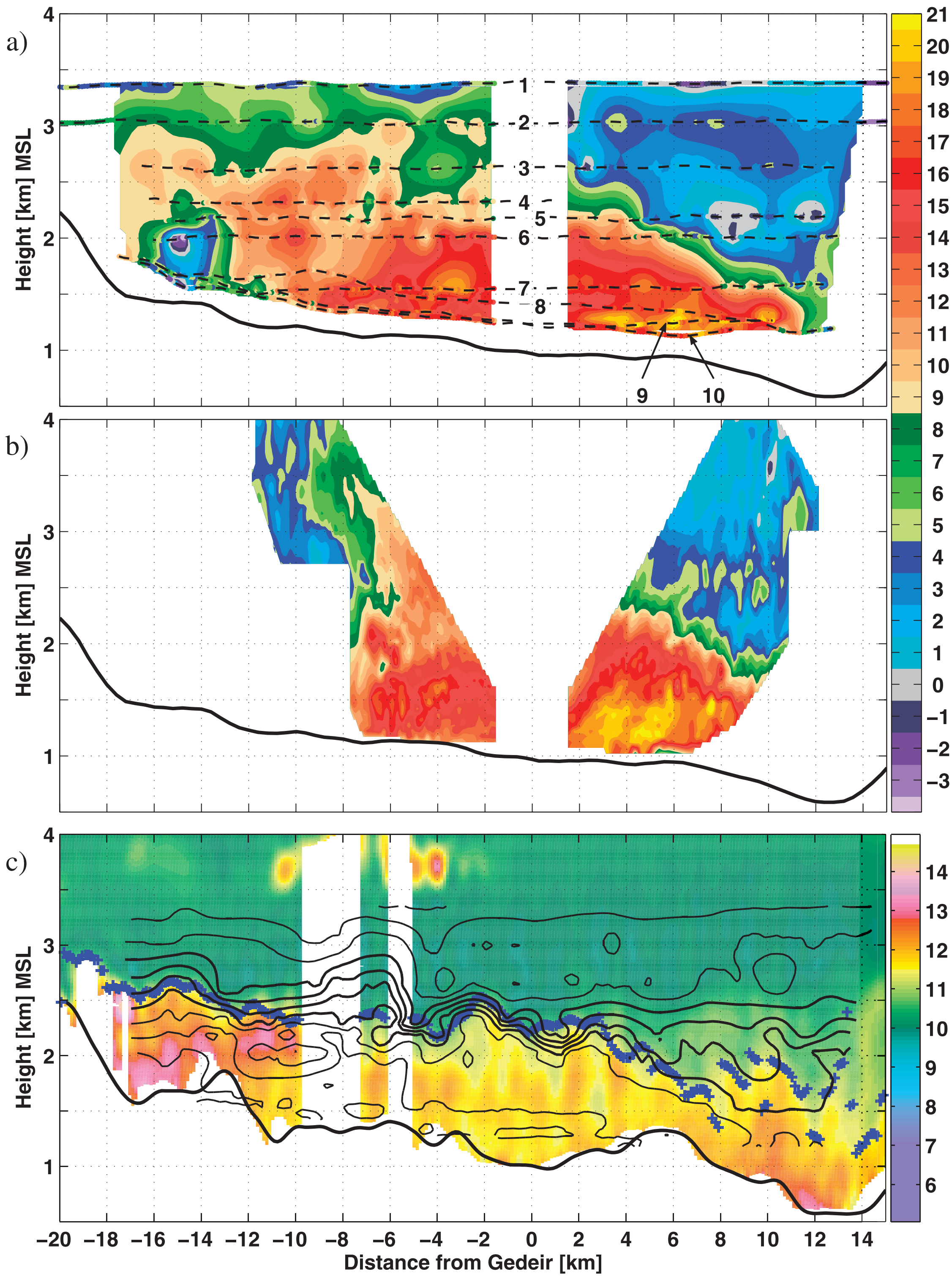

FIG. 5. Vertical cross section of (a) P3 and (b) TEACO2 lidar observations of the wind component parallel to the lidar beam. The heavy solid black line indicates the topography. The black dashed lines in (a) show the locations of the P3 flight legs; colored dots along those legs show the actual P3 pointwise measurements using the same scale as the contoured fields. The flight legs are labeled 1 through 10, starting from the top. (c) Vertical cross section of SABL relative backscatter intensity, with isentropes contoured at every 1 K interpolated from observations along the P3 flight legs. Bold isentropes (294–297 K) indicate the elevated inversion. Blue crosses mark the top of the aerosol mixed layer derived from the SABL data.

As shown in Fig. 5c, the top of the aerosol mixed layer determined from the SABL data closely coincides with the isentropes that make up the elevated inversion at almost all locations where the inversion is strong and well defined. Such good agreement is consistent with Flamant et al. (2002), who found that the top of the aerosol mixed layer in the Wipptal, as measured by a different lidar, the LEANDRE 2 was also collocated with the inversion during the 30 October 1999 foehn case. In the region where the inversion is not well defined (5–6 km downstream of the lidar), where isentropes separate and overturn, the top of the aerosol mixed layer appears to reflect the influence of such mixing in that it is more varied and broken up.

The dropsonde fell through the region of interest (from 4 km MSL to the ground) in roughly 10 min, and the sounding from Gedeir ascended from the ground to 4 km MSL in about 13 min, so these soundings taken at approximately 1200 UTC provide additional checks on the stationarity of the flow. In Fig. 6 the dropsonde and Gedeir soundings are compared with the potential temperature and wind profiles obtained from the interpolated P3 data at the same locations along the valley axis where the sondes reached or left the ground. As shown in Fig. 1a, both sondes were blown a significant distance down the valley as they transited between the surface and 3.5 km MSL, so comparing their observations to those at individual vertical profiles taken from the P3 cross section is necessarily somewhat qualitative. Nevertheless, the elevation and strength of the inversion agree nicely with the P3 profiles at both locations. The P3-interpolated thermodynamic sounding at Gedeir does show an unstable lapse rate between 2.6 and 3 km MSL, where the radiosonde reports a stable stratification similar to that recorded further upstream by the dropsonde. We believe the unstable lapse rate is spurious and arises from the large time offset between flight track 2 (at the 3-km level MSL) and the other P3 flight legs.[3] The P3-derived wind profile is in reasonably good agreement with the Gedeir sounding. The details of the layer structure in the wind field observed by the dropsonde are, however, not particularly well captured by the P3 data.

In summary, the preceding comparisons verify that the interpolated fields from the P3 in situ measurements closely match almost all the observations from the TEACO2 Doppler lidar, the SABL, the dropsonde, and the Gedeir radiosonde. This good agreement confirms that the flow was relatively steady throughout the duration of the P3 observations and supports the use of the P3 cross-sectional data for more detailed analysis.

[3] Despite the time offset, flight track 2 is retained in our analysis to fill the 750-m-deep gap between the levels of tracks 1 and 3.

5. Analysis of the full P3 dataset

As a first step, the P3 observations of velocity and potential temperature were split into a local mean value and a turbulent fluctuation. The P3 data are collected at a frequency of 1 Hz, which gives approximately one data point every 120 m along the flight track. The mean fields (denoted by overbars) are the average of the observations from the 17 consecutive points along the flight, centered at the point in question. The turbulent fluctuation (denoted by primes) is the difference between that mean and the observation. The 17-s period, which yields bins roughly 2 km wide, is approximately equal to the half-wavelength of the major undulations on top of the inversion layer.

a. Mean winds and isentropes

Vertical cross sections of the local mean along-gap velocity component $\bar{u}$ and potential temperature $\bar{\theta}$, interpolated using (1), are plotted in Fig. 7. The along-gap wind was defined as the component of the horizontal wind vector aligned with the average orientation of the valley axis (azimuth angle of 342°), which is positive in the northward direction. As shown in Fig. 7 (and also evident in the sounding data in Fig. 2), the airflow through the Wipptal had a two-layer structure in which relatively well-mixed fluid in a strong southerly flow was separated by an elevated inversion from flow aloft where $\bar{u}$ is much weaker. The inversion, whose height decreased northward from 2600 to 2000 m MSL, was below the elevation of the major surrounding peaks.

Upstream of Gedeir, at approximately $x = -6$ km, the inversion dips downward and the wind speed increases in the lower layer. Another similar but less pronounced feature is evident at $x = -14$ km. Further downstream (around $x = 4$ km) the inversion weakens and the isentropes separate and overturn; the jet of fast airflow remains near the ground, but the flow aloft inside the region of low stratification is much weaker and even reversed. The average wind speed below the inversion increases by roughly 10 m s^{-1} between $x = -15$ and +5 km, which is the portion of the valley where the inversion layer is most well defined. Even though there are some pronounced undulations of the isentropes, the average height of the inversion above the ground does not decrease in this portion of the valley. The best linear fits in the least squares sense of the bottom topography and the 295-K isentrope (which most closely follows the

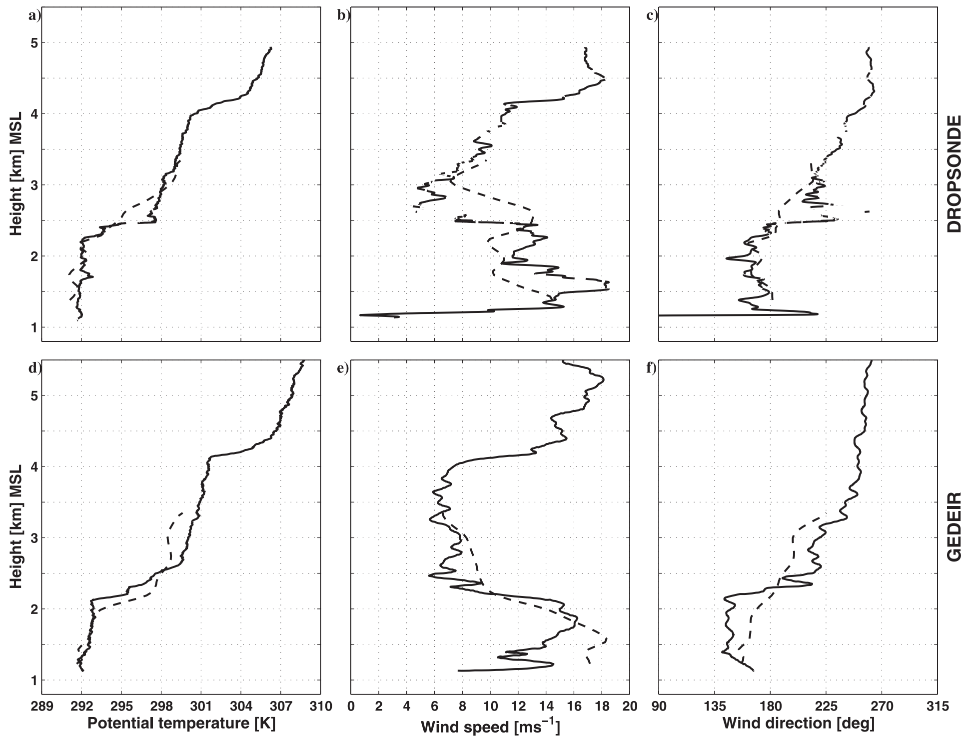

FIG. 6. (a) Potential temperature, (b) wind speed, and (c) wind direction from the dropsonde (solid lines) and the vertical profile taken from the interpolated P3 in situ measurements (dashed lines) at approximately the same location. (d)–(f) Same as (a)–(c), but for profiles at Gedeir.

top of the aerosol mixed layer) are indicated on Fig. 7; the two lines are almost perfectly parallel. The least squares fit to the terrain beneath the flight track falls 458 m between $x = -15$ and $x = 5$ km.[4]

Because the depth of the high-speed flow along the axis of the Wipptal is not decreasing as the flow accelerates, mass cannot be conserved unless air is subsiding from aloft or converging laterally into the region of high winds. One possibility is that cross-valley circulations were fed by air in the tributary valleys emptying into the Wipptal. Although surface winds may not be representative of the flow aloft, they are the only data available in the tributary valleys on 20 October 1999, and those winds were very weak. For example, one station in the Stubaital (see Fig. 4 for location) did not record winds in excess of 0.3 m s^{-1} during the whole foehn event. Before attempting to further assess the cross-valley circulation, we will examine evidence suggesting that—at least with respect to motions in the plane of the P3 cross section—air is subsiding into the flow from aloft.

The transport by the mean velocities ($\bar{u}$, $\bar{w}$) across the location of each mean isentrope is characterized in Fig. 8. The dashed lines in Fig. 8 show the vertical displacement $z_{\bar{\theta}}(x)$ of each mean isentrope as a function of distance downstream from $x = -15$ km for $\bar{\theta} = 293, 294, \ldots, 299$ K. The cumulative displacement δ_k that would be produced by a parcel *moving with the velocity at each point on the* $\bar{\theta}_k$ isentrope beginning at $x = -15$ km,

$$\delta_k(x) = \int_{-15}^{x} \frac{\bar{w}(\tilde{x}, z_{\bar{\theta}_k})}{\bar{u}(\tilde{x}, z_{\bar{\theta}_k})} d\tilde{x},$$

is shown by the thin line.[5] If the local mean flow were steady, adiabatic, confined to the plane of the vertical

[4] If the terrain is averaged perpendicular to the track over distances of 2, 3, or 4 km and lines are fit to those averaged topographies, the drops are 480, 431 and 373 m, respectively. Shifting the average so that it is 80% to the west and 20% to the east of the track, as in Armi and Mayr (2007), gives values for these widths of 406, 419, and 472 m, respectively. The 10-km-wide averaging distance used in Armi and Mayr (2007) drops 510 m, but 10 km is substantially wider than the width of the high-speed gap flow suggested by the lidar cross sections (cf. Fig. 11). Because 458 m is near the mean of these other values, we will estimate the slope of the topography using the profile below the flight track.

[5] These thin lines are not trajectories. Trajectories in the 2D vertical cross section show moderately more descent, but their utility in the turbulent region below the inversion is unclear.

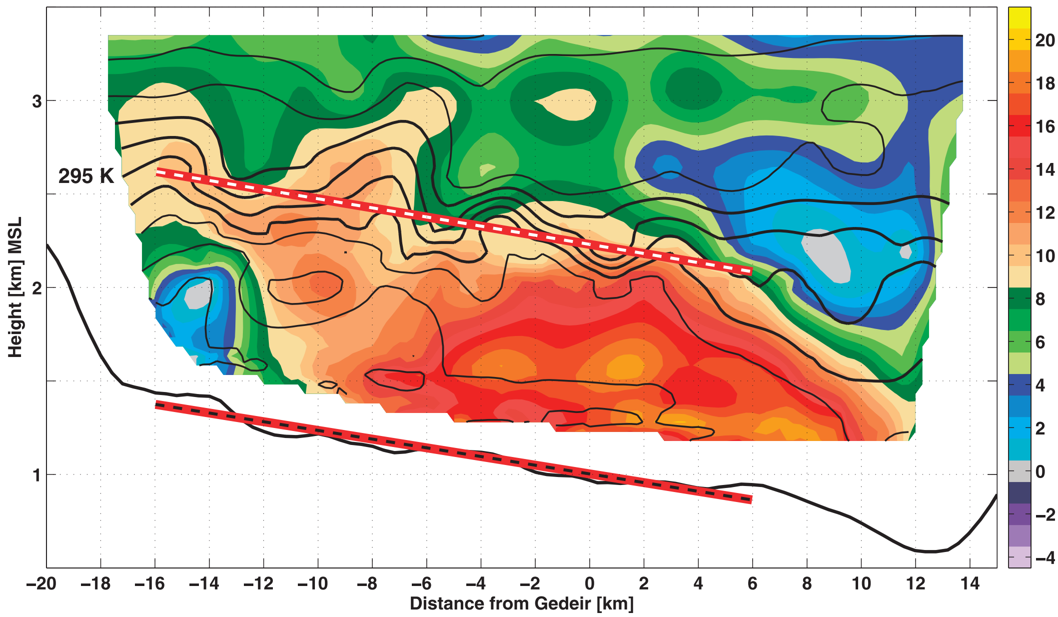

FIG. 7. Vertical cross section through the Wipptal along the average P3 flight track showing $\bar{u}$ (color contours) and $\bar{\theta}$ (black lines at 1-K intervals). Bold lines highlight the 294–297-K isentropes in the core of the inversion. Thick black line at the bottom indicates the terrain along the cross section. The white (black) dashed line on the red background is least squares fit to the 295-K isentrope (topography) over the region $-15 \leq x \leq 5$ km.

cross section, and perfectly observed, $\delta_k(x)$ would be identical to $z_{\bar{\theta}_k}(x) - z_{\bar{\theta}_k}(-15)$ but, as is apparent in Fig. 8, the two can be very different. The cumulative displacement relative to that of the isentrope at $x = 5$ km, $\Delta z = \delta(5) - z_{\bar{\theta}}(5) + z_{\bar{\theta}_k}(-15)$ is noted at the left of each isentrope.

The values of Δz for $\bar{\theta} = 293$, 294, and 295 K suggest the presence of velocities capable of producing downward isentrope-relative vertical displacements similar in magnitude to the displacement of the isentrope itself. The downward isentrope-relative displacements are much smaller farther aloft, except for $\bar{\theta} = 298$ K. Both the precise location of the 298-K isentrope and the velocity fields along that isentrope are strongly influenced by the data collected along flight leg 2. As mentioned in connection with Fig. 6, leg 2 was flown 1.5 h earlier than the other legs; when it is incorporated in our objective analysis of the θ field, the data from this leg incorrectly produce an unstable lapse rate in the vicinity of Gedeir between 2.6 and 3 km MSL. We believe the large Δz associated with the 298-K isentrope is not representative of the actual flow; rather, it is an artifact of the time offset associated with the data collected on flight leg 2.

It is hard to place any meaningful bounds on the errors in Δz, particularly because we were not able to find up-to-date estimates of the accuracy of the vertical velocity measurements by the P3. Note that there does not appear to be any downward bias in the P3 vertical velocities. As an example, consider the highest flight leg (track 1), which extends well north and south of the Wipptal. An air parcel moving at the average horizontal and vertical velocity along the 52-km length of track 1 would ascend 94 m.

If we continue to neglect 3D effects (and continue to accept the flow as steady), the mean advection of potential temperature must be offset by the divergence of the turbulent heat fluxes, which (neglecting horizontal turbulent fluxes) implies that

$$\bar{u}\frac{\partial\bar{\theta}}{\partial x} + \bar{w}\frac{\partial\bar{\theta}}{\partial z} = -\frac{\partial}{\partial z}\overline{w'\theta'}, \quad (2)$$

where as before, the overbar denotes the average over 17 consecutive data points. The regions of strongest cross-mean-isentrope flow, where the magnitude of $w_\perp = d(\delta - z_{\bar{\theta}})/dt$ exceeds 1 m s^{-1}, are shown in Fig. 8 by the thick segments on top of $\delta(x)$; gray (black) indicates negative (positive) values of $w_\perp$. Most of the rapid descent takes place in the region $-7.5 \leq x \leq -4$ km, which is the same region where the largest wave is apparent in the isentrope field in Fig. 7. A second region of significant negative $w_\perp$ is found near $x = -14$ km, which is the location of the next strongest wave in the flow. The $w_\perp$ near $x = -14$ km are, however, only about 1/3 as strong as the $w_\perp$ in the larger wave at $x = -5.5$ km.

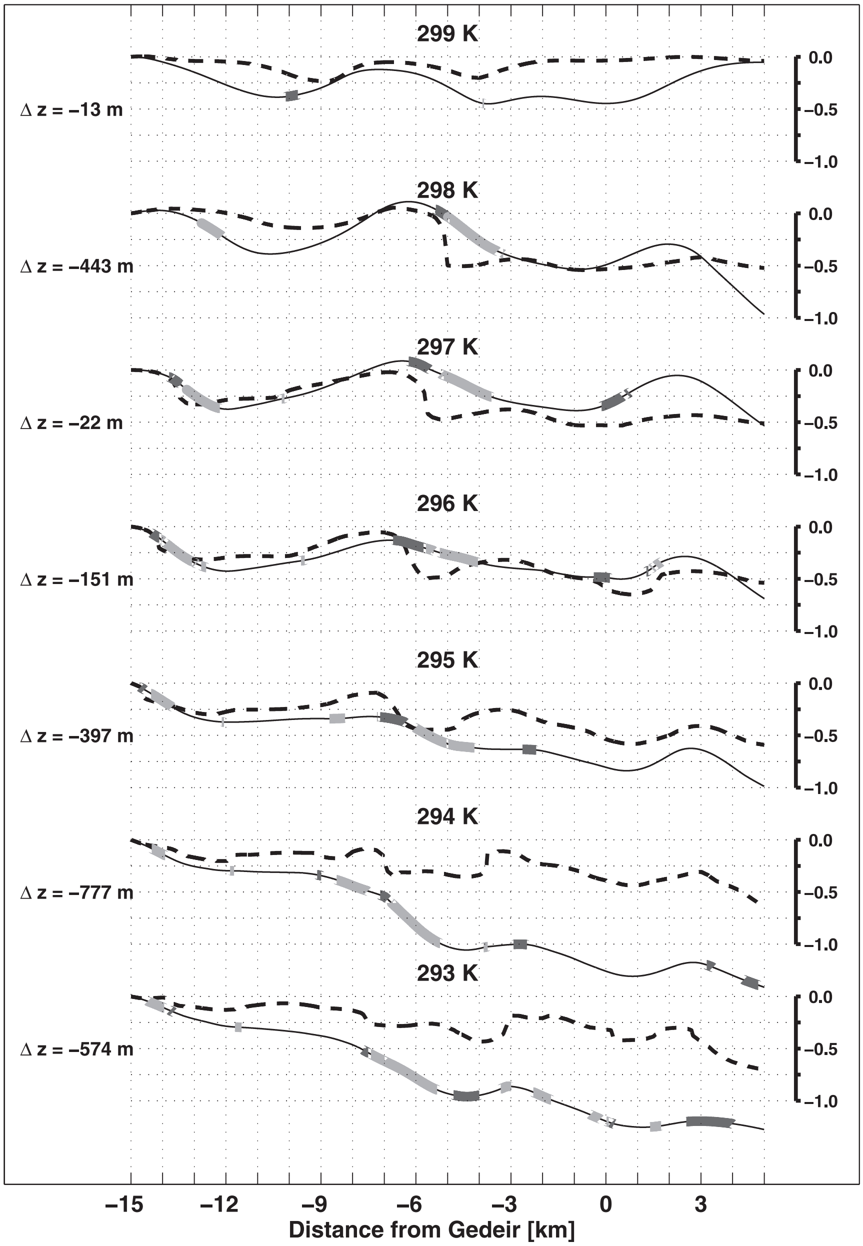

FIG. 8. Heavy dashed line is the vertical displacement of each isentrope as a function of distance downstream from $x = -15$ km. Data are plotted for mean isentropes $\bar{\theta} = 293$–299 K with individual vertical scales in km at the right. Thin lines show $\delta(x)$ for each isentrope, with the total displacement Δz noted at the left. Thick gray (black) segments indicate locations where the mean-field cross-isentrope velocity $w_\perp$ is more negative (positive) than -1 (1) m s^{-1}.

The intensity of the turbulent heat fluxes along each flight track is shown in Fig. 9. To focus on the regions of strongest heat fluxes, the colored dots show the extreme value of $\overline{w'\theta'}$ in each five-data-point-wide segment (plotted at the center of the segment); no dot is plotted for segments in which $\max(|\overline{w'\theta'}|) < 0.1$ km s^{-1}. The turbulent fluxes are largest in the vicinity of the inversion and are on average slightly negative. The strongest vertical turbulent heat flux divergences are found near the wave at $x = -5.5$ km. If one attempts to evaluate (2) near the base of the trough in this wave[6] by finite differencing the P3 data along flight tracks 4 and 5, the net advective forcing [LHS of (2)] varies smoothly with x

[6] At about $z = 2.2$ km MSL in the region $-7.5 \le x \le -4$ km.

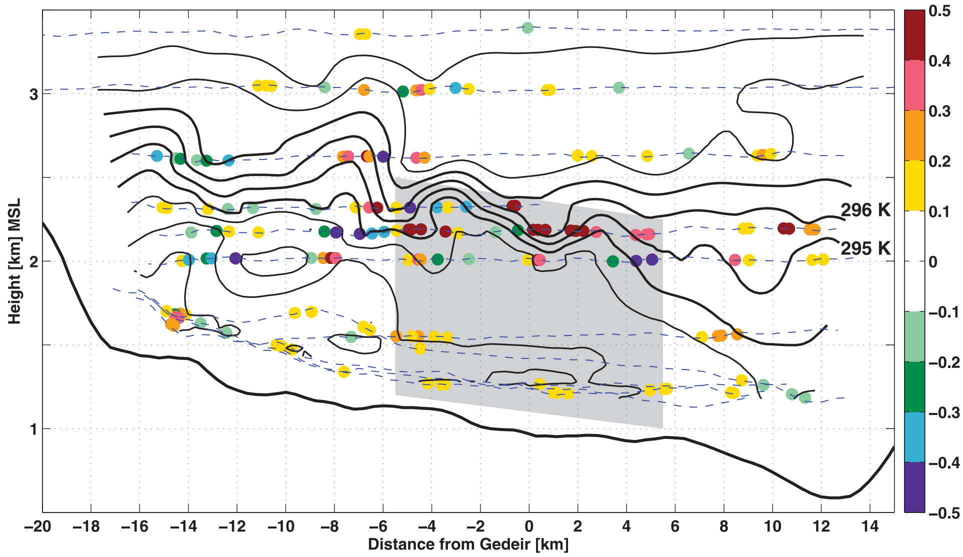

FIG. 9. Vertical cross section of turbulent heat flux $\overline{w'\theta'}$ (colored dots in m K s^{-1}) plotted along the individual P3 flight tracks, indicated by the dashed blue lines. Overplotted in solid black lines are contours of potential temperature (every 1 K) obtained by interpolating the P3 data. Isentropes plotted in thicker black lines (294–297 K) highlight the core of the elevated inversion. Shaded parallelogram shows the projection of the mass budget volume onto the x–z plane. Thick solid line at the bottom shows the topography.

whereas the turbulent heat flux divergence is negative (cooling), but quite noisy.[7] The right- and left-hand sides of (2) do have similar magnitudes at several points, but the x-averaged turbulent heat flux divergence is an order of magnitude smaller than the x-averaged net advective forcing.

One possible explanation for the noisiness and smallness of the turbulent heat divergence is that the turbulence is undersampled by the 1-Hz P3 data. For example, isotropic eddies with length scales equal to the thickness of the inversion (300–400 m) are likely to produce significant heat transport but will not be accurately resolved in the P3 data, which are only available every 120 m. The extent to which the magnitudes of the turbulent heat fluxes might increase if these eddies were accurately sampled is unknown.

The strength of the turbulence in this event may be compared to other estimates of turbulence in severe orographically forced circulations by examining the vertical velocity variance $\overline{w'^2}$. Smith (1987) calculated maximum $\overline{w'^2}$ ranging between 8 and 15 m^2 s^{-2} from 1-Hz data collected during P3 flights through several Croatian bora events. Smith averaged over 10-s intervals, in comparison to the 17-s intervals used here. Doyle and Durran (2002) computed maximum turbulent kinetic energy (TKE) values of roughly 13 m^2 s^{-2} from numerical simulations of mountain-wave-induced rotors, although they included all three wind components, $(\overline{u'^2} + \overline{v'^2} + \overline{w'^2})/2$, in their TKE calculation. In our case the largest values of $\overline{w'^2}$ are found near the surface, especially in the upper part of the Wipptal where the maximum exceeds 9 m^2 s^{-2}. Nevertheless, the turbulence extends throughout the layer and, as shown in Fig. 9, the turbulent heat fluxes are strongest near the inversion, where the gradients in θ are larger than near the surface. Above the inversion the turbulence is much weaker.

b. Cross-valley circulations

We hypothesize that the primary factor responsible for the failure of the P3 observations to satisfy (2) is undersampling of the turbulence by the P3. An important alternative explanation is that the turbulent heat fluxes were in fact small and the cross-gap component of the potential temperature advection kept the 3D flow isentropic, which assuming steady flow, would require

$$v\frac{\partial\theta}{\partial y} = -\mathbf{u}_{xz} \cdot \nabla_{xz}\theta, \tag{3}$$

where $\mathbf{u}_{xz}$ and ∇_{xz} are the velocity vector and the gradient operator in the plane of the P3 cross section, and v

[7] The turbulent heat flux divergence does force warming closer to the surface.

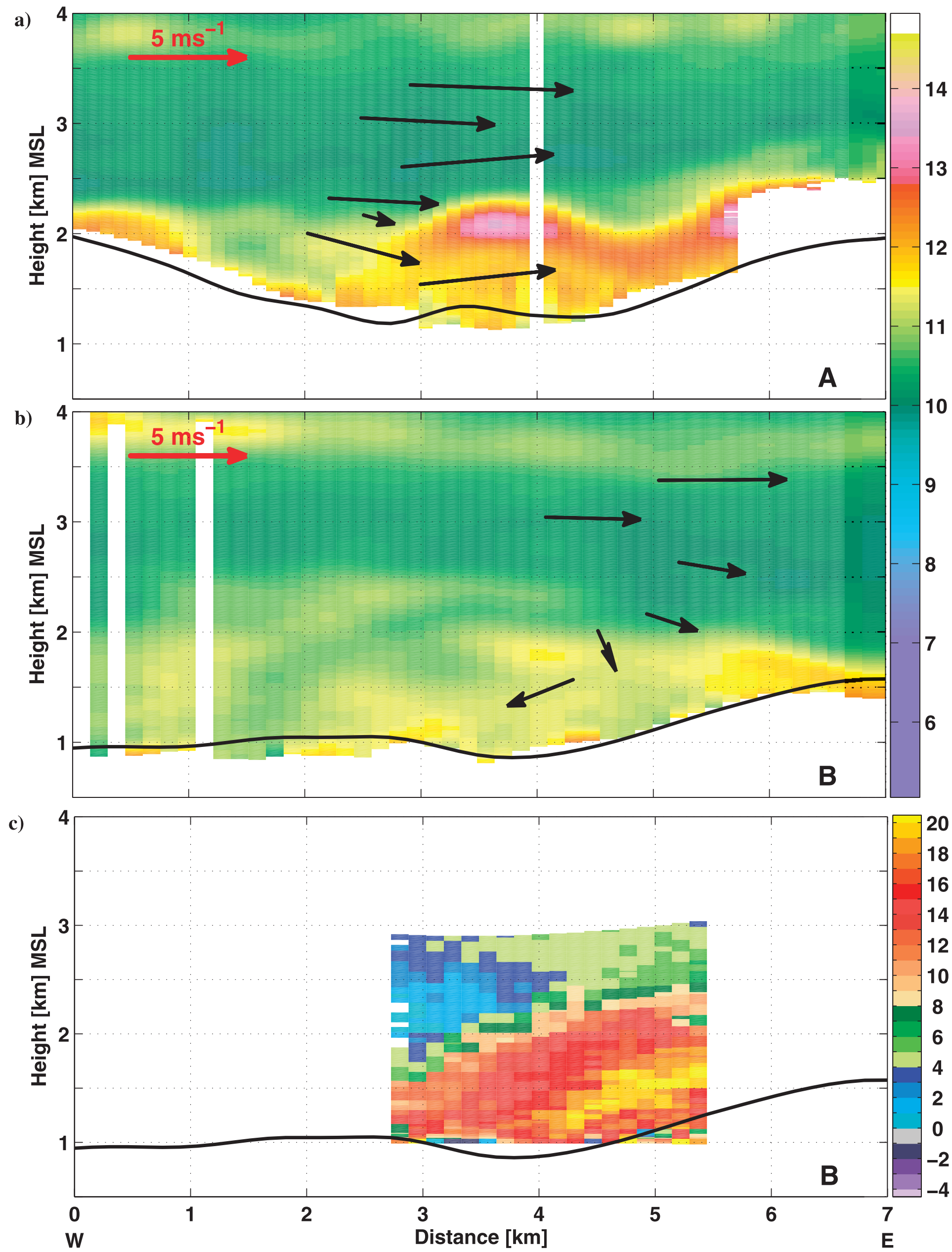

FIG. 10. Vertical cross sections of SABL backscatter intensity, with P3 in situ measurements of the velocity in the plane of the cross section shown by the bold vectors. The tail of each vector is plotted at the location of the P3. The thick solid line is the terrain; white areas indicate either missing data or the locations where the SABL signal was obscured by the terrain or clouds. (a),(b) Cross sections A and B, respectively, as indicated in Fig. 1a; (c) a vertical slice along cross section B through a TEACO2 lidar volume scan of radial velocity (m s^{-1}, positive into the page) collected at approximately 1320 UTC.

and y are the velocity and coordinate perpendicular to the axis of the gap (positive toward the west-southwest). The cross-gap wind component observed by the P3 was relatively small throughout the valley and predominately toward the east. It reached maximum values of about -6 m s^{-1}, and the average for all of the P3 flight tracks below the inversion layer was -1.1 m s^{-1}. There are no direct observations of the cross-gap potential temperature profiles, but a qualitative indication sufficient for our purposes can be gleaned from the SABL and TEACO2 lidar data. Figures 10a,b show vertical cross sections at two different locations in the Wipptal: 11.2 km upstream of Gedeir (section A) and 4.8 km downstream (section B). Also plotted in Figs. 10a,b are the in situ winds observed by the P3 in the plane of the cross section.

The SABL data from cross section A show a layer of relatively high aerosol concentration that deepens to the east of the P3 flight tracks. The highest wind speeds and lowest potential temperatures lie within the aerosol layer in the along-valley section in Fig. 5c and almost certainly do so in this cross-valley section as well. Thus, it appears that like the vertical winds, the cross-valley winds blow across the inversion from warm potential temperatures to cold, which is precisely opposite to what would be required if the cross-valley circulation were to compensate for the vertical subsidence and allow the 3D flow within the inversion layer to follow an isentropic surface. In mathematical terms, the right-hand side of (3) is positive (because, as projected onto the x–z plane, parcels cross isentropes from warm to cold), whereas the left-hand side is negative.

A roughly similar picture emerges along cross section B. The high-speed flow again lies along the eastern side of the Wipptal, as confirmed by the TEAC02 Doppler lidar scan for the same cross section in Fig. 10c (see also Fig. 4). Consistent with the along-valley SABL leg (Fig. 5c), the aerosol layer is more broken up and less clearly defines the top of the high-speed flow. Nevertheless, there are higher aerosol concentrations on the eastern side of the valley, so the horizontal potential temperature gradients near the level of the inversion layer are likely to be either flat or positive (higher potential temperature air to the west). Thus, except for the data point from the lowest flight track, all the P3 wind observations in the cross-valley plane are again in the wrong sense to compensate for the inversion-relative subsidence and keep the air parcels flowing along an isentropic surface. The downward and westward velocity on the lowest flight leg is an exception and would be in an appropriate sense to produce such compensation but, as clearly indicated by the TEACO2 radial wind data in Fig. 10c, this point is deep in the high-speed flow and thus below the inversion layer.

6. Characterizing $w_\perp$ from the Doppler lidar data

As noted in connection with Fig. 7, the wind speed below the inversion increases substantially while the average height of the inversion above the ground remains roughly constant. An estimate of the net mass flux divergence produced by the along-valley flow, and of the average vertical velocity required to balance this divergence, can be obtained by examining cross sections of radial velocity observed by the Doppler lidar at Gedeir. We take the top of the volume for the mass budget calculation as a plane following the mean slope of the isentropes in the inversion, thereby allowing a rough estimate of the subsidence in the vicinity of the inversion that would be required to satisfy mass balance. Because no information is available to determine the full 3D structure of the inversion layer or the cross-valley mass fluxes, our estimate is not intended to provide a definitive description of the actual mass balance but rather to give an order-of-magnitude value that can be compared with the values of $w_\perp$ derived independently from the P3 data.

Cross sections perpendicular to the mean along-valley flow (directed toward 342° azimuth) are shown in Fig. 11. The velocities plotted in Fig. 11 are adjusted under the assumption that the true wind vector is directed down valley and the lidar is sensing the component of that vector directed toward the instrument. The locations of these cross sections, which are 5.5 or 6 km upstream and downstream of the lidar, are shown in Fig. 4. The region of high-speed flow is not completely captured in these cross sections, but noting that the east wall of the Wipptal is generally much higher than that suggested by the topography in Figs. 11a,c,e, it is likely these cross sections include a significant fraction of the gap flow.

The upstream observations are somewhat noisy and do not clearly delineate the top of the high-speed flow. Downstream, the observations are much less noisy, and the top of the high-speed flow is near 2.25 km MSL. Taking 2.25 km as the top of the downstream budget volume and assuming that the top of this volume follows the mean slope of the isentropes in the inversion, the top of the upstream budget volume is taken as 2.5 km MSL. The top of each volume is indicated by the horizontal dashed black line in each panel of Fig. 11; the horizontal projection of the dashed lines onto the topography is shown in Fig. 4, and a side view of the $-5.5 \leq x \leq 5.5$ budget volume is shown by the shading in Fig. 9. The mass fluxes through the upstream and downstream faces of the budget volumes were computed by summing the flux for the individual pixels in each cross section. The net divergence was then used to calculate the average vertical velocity through the top of each budget volume required to close the mass budget without any contribution from cross-valley circulations.

Vertical velocities of -0.49 and -0.39 m s^{-1} through the top of the $-5.5 \leq x \leq 5.5$ budget volume would balance the net horizontal mass divergence of the along-valley flow at the earlier (Figs. 11a,b) and later (Figs. 11c,d) times, respectively. These may be compared with averages of $w_\perp$ over the same x interval of -0.31 and -0.34 for the 295- and 296-K isentropes, respectively. A vertical velocity of -0.46 m s^{-1} would balance the divergence in the slightly larger $-6 \leq x \leq 6$ budget volume, and this should be compared with $w_\perp$ averages

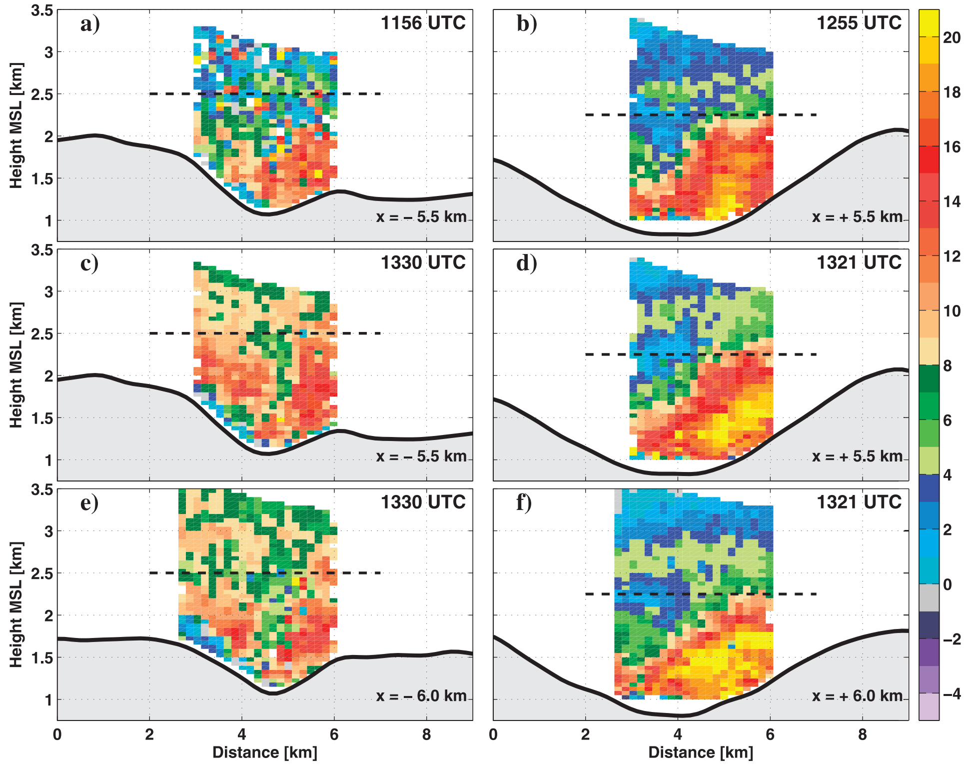

FIG. 11. Cross sections of estimated along-valley velocity in planes perpendicular to the flow: (a)–(f) 1156–1321 UTC. The distance north of Gedeir appears in the lower right of each panel, and the time of the scan in the upper right. Dashed horizontal lines denote the top of the volume used in the mass flux calculations; the horizontal projections of these lines are plotted in blue to show the position of each cross section in Fig. 4. Thick solid line and gray shading at the bottom shows the topography.

over the same interval of -0.38 and -0.29 for the 295- and 296-K isentropes.

The values of $w_\perp$ range between 50% and 80% of the velocities required to balance the along-gap divergence entirely by vertical motions. Cross-valley circulations are likely to play a role as well. The average v in the plane of the P3 cross section over $-6 \le x \le 6$ km is -0.77 m s^{-1}. The Δv across the sides of budget volume required to entirely balance the along-gap divergence is -1.6 m s^{-1}, which could be achieved in a manner consistent with the value obtained for the average v (approximately -0.8 m s^{-1}) in the P3 cross section if the average v varied linearly between zero on the east side of the flow nearest to the topography and 1.6 m s^{-1} on the west face of the 3.5-km-wide budget volume.

The available data are inadequate to determine the relative roles played by vertical and lateral mass fluxes. Nevertheless, from a theoretical viewpoint, we note that downward mass fluxes might be better able to support the high-speed gap flow if the potential energy of the subsiding air were converted to kinetic energy. Such conversion would reduce the loss of down-valley momentum that would tend to occur as mass is fluxed laterally into the jet. Both numerical simulations and future observations might help determine the relative roles of vertical and lateral mass fluxes in the mass balance for accelerating gap winds.

7. Conclusions

It is now well established that most of the air contributing to gap winds in the Wipptal descends from a level well above the Brenner Pass instead of squeezing through the pass itself (Mayr et al. 2004; Flamant et al. 2002; Armi and Mayr 2007), and this is certainly the case on 20 October 1999. Furthermore, it appears significant subsidence continued to occur at the level of the inversion, capping the gap flow well downstream of the Brenner Pass. The primary evidence for such subsidence comes from the analysis of in situ P3 observations.

As a first step, we verified that the interpolated wind and potential temperature fields measured on the P3 match very well with the observations from other platforms in the Wipptal: the wind speed retrieved by the TEACO2 lidar, the aerosol concentration obtained from the SABL lidar, and the dropsonde and radiosonde data. This agreement suggests that the P3 data, which were collected along multiple flight tracks over a 3-h period, can be used to reconstruct a vertical cross section that reasonably approximates the instantaneous flow along the valley axis.

The winds and potential temperatures observed by the P3 were objectively interpolated onto a vertical cross section, which was in turn interpolated to give the wind within the cross section along each isentrope. The displacement δ_k that would be produced by an air parcel moving with the $x-z$ velocity at each point on a particular isentrope was then compared with the vertical displacement of that isentrope over a 20-km-long segment along the Wipptal. If the flow were steady, 2D, and isentropic (and perfectly observed), δ_k would be identical to the cumulative displacement of the isentrope. The δ_k for the isentropes in the lower part of the inversion are, however, roughly double the actual downward displacement of the isentropes themselves, suggesting that at least within the plane of the cross section, air is descending across the time-mean position of the inversion. On the other hand, the δ_k for isentropes above the inversion matched the actual cumulative displacement of the isentrope much more closely (except for the 298-K isentrope). The cross-valley velocities measured by the P3, together with the aerosol data from the SABL lidar, suggest that the cross-valley winds blow opposite to the direction required for the full 3D flow to remain isentropic, thereby supporting the conclusion that air was indeed subsiding across the mean location of the isentropes in the inversion.

The -0.3 to -0.4 m s^{-1} downward isentrope-relative velocities obtained from the P3 data would be capable of providing 50% to 80% of the mass flux required to compensate for the along-valley mass flux divergence in a 3D volume centered on the location of the TEACO2 lidar. Because of a lack of information about the cross-valley circulations, the mass budget based on the Doppler lidar data does not determine how much inversion-level subsidence actually occurred. Nevertheless, it is encouraging that these two essentially independent analyses suggest similar values.

One important observation that is not consistent with the evidence for significant inversion-level subsidence is the weakness of the turbulent heat flux, which appears to be roughly one tenth of that required to compensate for the warming associated with the downward advection of θ relative to the mean position of the inversion. The 120-m resolution of the turbulence data collected by the P3 is too coarse to correctly capture fluxes by eddies on the scale of the 300–400-m-deep inversion layer. Such eddies could transport significant heat, and we believe their omission is the most likely reason that the heat budget does not close. Future observational campaigns devoted to the study of gap flow should try to include higher-frequency turbulence measurements and more sampling of cross-gap circulations.

Upon first inspection, the flow in the Wipptal on October 20 might be expected to be a good candidate for the application of reduced-gravity shallow-water theory: the surface layer was well mixed and capped by a strong elevated inversion, and the jet of fast flow below the inversion was relatively uniform and decoupled from the airflow aloft by a layer of directional wind shear. Nevertheless, our analysis suggests that the inversion capping the gap flow did not behave as a material surface, as envisioned in the RGSW model; rather, air at the inversion level sinks at roughly twice the rate required to follow the inversion itself. If such significant cross-inversion transport is found to be characteristic of typical gap flows, it would likely require a modification of the conventional RGSW gap-flow paradigm.

Our finding of downward transport at the level of the inversion is qualitatively consistent with that of Lackmann and Overland (1989). They estimated the entrainment velocity across a 6-K inversion bounding the top of a well-mixed gap-wind layer in the Shelikof Strait to be -0.02 m s^{-1}. Somewhat curiously, they also present an equation for the average large-scale vertical velocity at the inversion base but do not give its value. They emphasize the importance of entrainment at the level of the inversion in their mass and momentum budgets.

It would be interesting to examine other MAP events in which gap flows were capped by strong inversions to see whether the data suggest that significant subsidence is associated with those inversions. The 20 October case seems to be unique from a data analysis perspective, however, because the agreement between the TEACO lidar winds and vertical cross sections synthesized from the P3 data is much better than on the other days with P3 flights in the Wipptal. It may be that the flow was subject to more rapid temporal fluctuations on the other flight days, which could prevent the synthesis of P3 data into vertical cross sections representing the actual flow at any given instant.

Acknowledgments. We are indebted to the many individuals who made the collection of this data possible during the MAP campaign; particularly noteworthy are Georg Mayr's organization of the MAP GAP subproject and the surface station network, Larry Armi's role as chief scientist on the P3 flight, Robert Banta and Lisa Darby's assistance with the TEACO2 lidar data, and comments from an anonymous reviewer. The authors' research was supported by National Science Foundation Grants ATM-0137335 and ATM-0506589.

REFERENECS

Arakawa, S., 1968: A proposed mechanism of fall winds and Dashikaze. *Pap. Meteor. Geophys.,* **19,** 69–99.

Armi, L., and G. Mayr, 2007: Continuously stratified flows across an Alpine crest with a pass: Shallow and deep foehn. *Quart. J. Roy. Meteor. Soc.,* **133,** 459–477.

Bougeault, P., and Coauthors, 2001: The MAP special observing period. *Bull. Amer. Meteor. Soc.,* **82,** 433–462.

Colle, B. A., and C. F. Mass, 2000: High-resolution observations and numerical simulations of easterly gap flow through the Strait of Juan de Fuca on 9–10 December 1995. *Mon. Wea. Rev.,* **128,** 2398–2422.

Dorman, C., R. Beardsley, and R. Limeburner, 1995: Winds in the Strait of Gibraltar. *Quart. J. Roy. Meteor. Soc.,* **121,** 1903–1921.

Doyle, J. D., and D. R. Durran, 2002: The dynamics of mountain-wave-induced rotors. *J. Atmos. Sci.,* **59,** 186–201.

Durran, D. R., T. Marić, R. M. Banta, L. S. Darby, and R. M. Hardesty, 2003: A comparison of ground-based Doppler lidar and airborne in situ wind observations above complex terrain. *Quart. J. Roy. Meteor. Soc.,* **129,** 693–713.

Flamant, C., and Coauthors, 2002: Gap flow in an Alpine valley during a shallow south foehn event: Observations, numerical simulations and hydraulic analog. *Quart. J. Roy. Meteor. Soc.,* **128,** 1173–1210.

Gohm, A., and G. J. Mayr, 2004: Hydraulic aspects of foehn winds in an Alpine valley. *Quart. J. Roy. Meteor. Soc.,* **130,** 449–480.

——, G. Zängl, and G. J. Mayr, 2004: South foehn in the Wipp valley on 24 October 1999 (MAP IOP 10): Verification of high-resolution numerical simulations with observations. *Mon. Wea. Rev.,* **132,** 78–102.

Jackson, P. L., and D. Steyn, 1994: Gap winds in a fjord. Part II: Hydraulic analog. *Mon. Wea. Rev.,* **122,** 2666–2676.

Lackmann, G., and J. Overland, 1989: Atmospheric structure and momentum balance during a gap-wind event in Shelikof Strait, Alaska. *Mon. Wea. Rev.,* **117,** 1817–1833.

Mayr, G. J., and Coauthors, 2004: Gap flow measurements during the mesoscale Alpine programme. *Meteor. Atmos. Phys.,* **86,** 99–119.

Pettre, P., 1982: On the problem of violent valley winds. *J. Atmos. Sci.,* **39,** 542–554.

Smith, R. B., 1987: Aerial observations of the Yugoslavian bora. *J. Atmos. Sci.,* **44,** 269–297.

Smith, W., and P. Wessel, 1990: Gridding with continuous curvature splines in tension. *Geophysics,* **55,** 293–305.

Weissmann, M., G. Mayr, R. Banta, and A. Gohm, 2004: Observations of the temporal evolution and spatial structure of the gap flow in the Wipp Valley on 2 and 3 October 1999. *Mon. Wea. Rev.,* **132,** 2684–2697.